INTERNATIONAL JOURNAL FOR NUMERICAL METHODS IN FLUIDS
Int. J. Numer. Meth. Fluids 2005; **49**:349–369
Published online 3 June 2005 in Wiley InterScience (www.interscience.wiley.com). DOI: 10.1002/fld.1000

Numerical validation of a stability model for a flexible over-expanded rocket nozzle

E. Lefrançois*,†

Laboratoire Roberval FRE2833, Université de Technologie de Compiègne, 60205 Compiègne Cedex, France

SUMMARY

A numerical approach for the aeroelastical stability of an over-expanded rocket engine is proposed in this paper. The main idea is to offer a better understanding of the repercussions likely to appear from the aeroelastic coupling in terms of side loads that may be responsible for damage effects on the engine. After a brief description of the stability model issued from previous works (Pekkari's team) and details upon a numerical fluid–structure coupling code, comparative calculations are conducted. The stability model is then called into question and a finer analysis is proposed to explain its major tendency to over-predict the aeroelastic frequency shift in comparison with numerical coupling results. Copyright © 2005 John Wiley & Sons, Ltd.

KEY WORDS: finite element; rocket nozzle; Pekkari's stability model; aeroelasticity

1. INTERESTS FOR THE STUDY

During the starting phase of a rocket engine, a first 'blast' wave may sweep the whole nozzle to initiate the flow. Behind that first pressure discontinuity, the flow gets established by adjusting to the outside pressure ratio. That phase corresponds to the existence of a matching shock pattern, of which the longitudinal position is governed by the pressure field (see Figure 1).

Undesirable effects are particularly strong at low-altitude flight where the external pressure is strongest and opposes itself to the flow [1]. Amongst them, we may cite side load effects that are due to a loss of symmetry of the flow (see Figure 2) whose origin is still kept out of understanding. Their effects may be strong enough to damage the engine and deviate the launcher trajectory.

*Correspondence to: E. Lefrançois, Laboratoire Roberval FRE2833, Université de Technologie de Compiègne, 60205 Compiègne Cedex, France.
†E-mail: emmanuel.lefrancois@utc.fr

Contract/grant sponsor: PILCAD — Plateforme Inter-Laboratoires de CAlcul Distribués
Contract/grant sponsor: University of Technology of Compiègne

Received 10 December 2004
Revised 31 March 2005
Accepted 24 April 2005

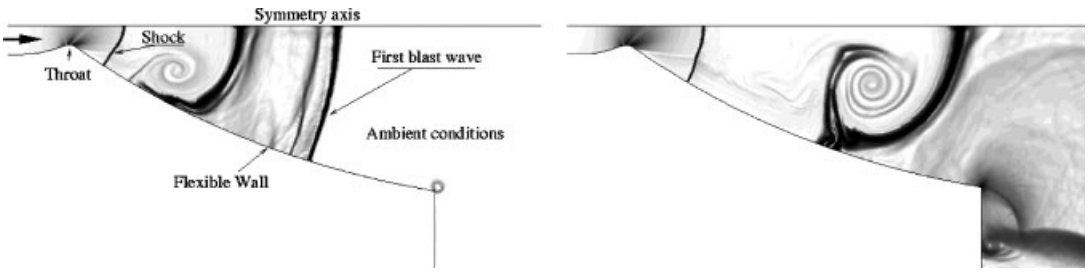

Figure 1. 2D numerical simulation of transient starting phase—numerical Schlieren.

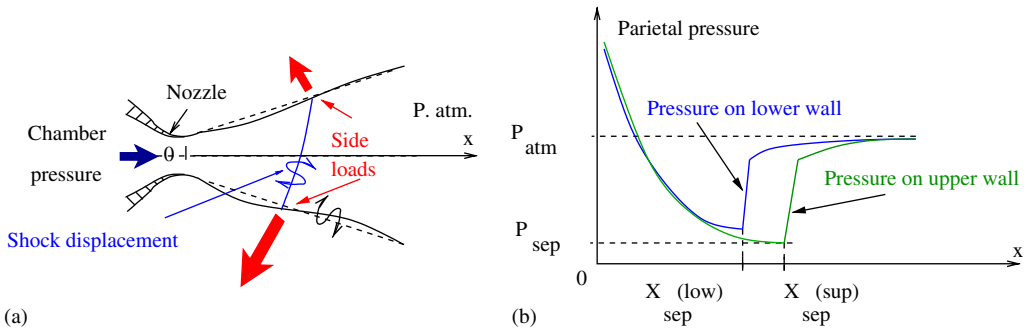

Figure 2. (a) Axial section of a rocket engine; and (b) parietal pressure profile.

This phenomenon is known for a long time since the first works according to this, date back to the 1920s, notably with Prandtl, Meyer and Stodola who worked on over-expanded jets (i.e. with presence of a separation shock) [2]. The interest increased in the sixties when the same phenomenon was observed on the J2S engine of the Saturn V launcher [3]. From 1960 to 1966, NASA undertook a vast program of research to better understand the physics of side loads. It led to numerous theories and a huge amount of experimental data for side loads. However, the exact understanding of the physics underlying such a phenomenon is still not totally clear and data correlations are complicated at best.

Today, this problem still appears in rocket engines such as the SSME of the American space shuttle [4], the Vulcain engine of the final version of Ariane V launcher [5–7] and other Japanese and Russian rocket engines.

The origin of the problem may be explained by the choice of the *design* in report with the performances and employed materials for the construction of the engine. On the one hand, the performances of a engine are directly linked to the thrust, proportional to the report of the sections of the exit and of the throat of the divergent. On the other hand, the weight being the principal concern in astronautics, the choice of materials more rigid and heavier would have in fact for principal drawback to decrease the payload in a notable manner and to reduce all profitability hope for the launcher.

Three possible causes of appearance of the side load effects currently keep the attention of the researchers [5]:

1. The pressure fluctuations in the separation and recirculation zones downstream the shock. The interest evocated by many laboratories of the European community is well expressed in Reference [5].
2. The transition between two kinds of separation flow: the *free separation shock* and the *restricted separation shock*. This transition may occur during the start-up process. Both cases lead to different wall pressure distributions that may generate side-loads if the symmetry is not ensured. This phenomenon has been experimentally and numerically observed [8, 9].
3. The aeroelastic coupling [10–12].

Aeroelasticity has been studied for at least forty years from a theoretical point of view [13–15] and more recently a numerical approach has been developed and proposed [16–18]. The development of coupled models for aeroelasticity is quite recent due to its multidisciplinary nature. Moreover, its application to rocket engines has rarely been studied [12, 19]. It seems reasonable for this case to focus on the structural aspect, the engine being above all, the 'organ' we wish to preserve.

The current studies conducted for the understanding of the likely effect of aeroelastic coupling on the side load effects sweep a rather wide range [5]. It appears that the first stability model for aeroelastic effects on flexible rocket engines was proposed by Pekkari [12]. Based on an extreme simplification of the parietal pressure profile of the flow, it notably made obvious the possible appearance of phenomena such as divergence (static instability) according to the position of the shock. This team notably reinforced the approach with many experimental measures on different engine configurations [10]. The current tendency concerns the validation of behaviour models as well as with the use of numerical tools [20, 21] than with experimental measures on flexible and reduced scale engines. It is realized in the framework of a European research group Flow Separation Control Device (FSCD) and a French research group Aérodynamique des Tuyères et Arrière-Corps (ATAC). This latter notably includes the CNES (French Space Agency) the SNECMA (Aerospace Propulsion and Equipment Group) and the ONERA (French Aeronautics and Space Research Center) [22]. This paper is the result of research activities supported by ATAC.

The main concern of the present work is to increase the understanding of the stability model. Previous works permitted to improve the model in taking into account both static (such as divergence) and dynamic instabilities (such as flutter) [20]. The objective is not to study specifically the aeroelastic effects on side loads, but to study the local behaviour of a flexible structure in response to a separation shock. The study domain will thus be restricted to a half divergent nozzle (see Figure 1). Moreover, the fluid is supposed inviscid in order to significantly reduce CPU cost comparatively to viscous cases. However, recent calculations including viscous and turbulent effects have shown a good agreement with the results presented in this paper [23].

A first part is dedicated to the presentation of the stability model from Pekkari's works [12] for a flexible rocket engine in the presence of a separation shock, model that has been improved. A second part is dedicated to the coupling numerical model composed of a structure and a fluid code. Parallel libraries are used to permit messages passing between the two calculation codes and to significantly reduce CPU cost for solving the fluid equations. Finally,

coupled calculations are presented in order to show the tendency of the stability model to over-predict the frequency shift. This confrontation will come to support a fourth and last part that will question the model and will propose an improvement in accordance with other current works [9].

2. AEROELASTIC STABILITY MODEL

In this section, we briefly introduce the general way to study the stability of a flexible structure in relation with external flows. In general, the finite element approximation of the equilibrium relation for a flexible structure leads to the system

$$[M]\{\ddot{W}\} + [C]\{\dot{W}\} + [K]\{W\} = \{F\} \tag{1}$$

where $[M]$, $[C]$ and $[K]$ are, respectively, the mass, damping and rigidity matrices. $\{W\}$, $\{\dot{W}\}$ and $\{\ddot{W}\}$ define the displacements, velocity and accelerations nodal vectors. $\{F\}$ defines the forcing vector resulting from the coupling with aerodynamics. The forcing term is usually decomposed as follows:

$$\{F\} = [K_{\text{aero}}]\{W\} + [C_{\text{aero}}]\{\dot{W}\} \tag{2}$$

The first term represents instantaneous structure response to the pressure distribution. The last term introduces a phase difference between both fluid and structure. Introducing Equation (2) in Equation (1), it leads to

$$[M]\{\ddot{W}\} + [C - C_{\text{aero}}]\{\dot{W}\} + [K - K_{\text{aero}}]\{W\} = \{0\} \tag{3}$$

2.1. Pekkari's stability model

Pekkari's model [12] finds its main contribution in the choice of the parietal pressure approximation of the flow that undergoes an expansion from the throat to the shock. The effect of the deformed wall due to the displacement $\mathbf{w}$ of normal derivative $\partial w_n/\partial s$ (s is the curvilinear coordinate along the engine wall), is taken into account by the so-called 'piston' theory [24] (cf. Figure 3(b)). Mathematically, the wall pressure $p(x, \mathbf{w})$ is then obtained in accordance

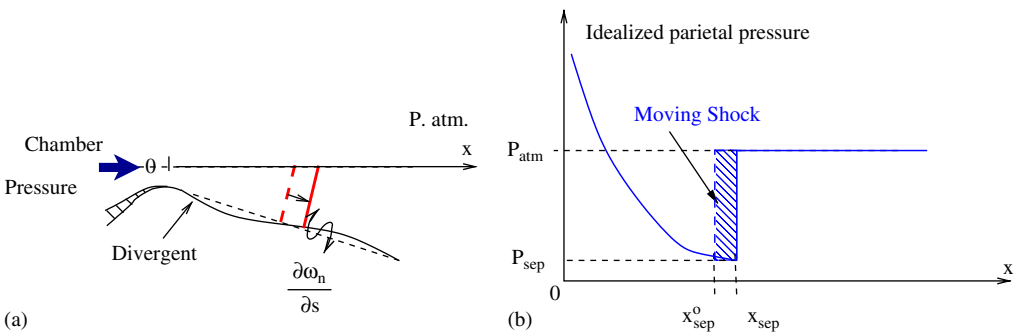

Figure 3. (a) Half over-expanded rocket engine; and (b) parietal pressure profile.

with the expressions:

$$p(x,\mathbf{w}) = \begin{cases} p_\infty(x) + \dfrac{\rho_\infty U_\infty^2}{\sqrt{M_\infty^2 - 1}} \dfrac{\partial w_n}{\partial s}, & x < x_{\text{sep}} \\ p(x_{\text{sep}}) = p_{\text{sep}}, \text{ such as } \eta = \dfrac{p_{\text{sep}}}{p_{\text{atm}}} = 1/15, 1/16, \ldots & x = x_{\text{sep}} \\ p_{\text{atm}}, & x > x_{\text{sep}} \end{cases} \tag{4}$$

where $p_\infty(x)$ is the static pressure resulting from the gas expansion (extracted from expansion flow or shock tables), p_{atm} is the atmospheric pressure. The following variables ρ_∞, U_∞ and M_∞, respectively, define the local values of the density, the axial velocity and the Mach number. From this analytical pressure profile, a normal shock is considered at location x_{sep} by using a separation criterion (designed by η) such as Schmucker criterion [3].

This study being dedicated to a stability analysis, only aerodynamics loads resulting from shock displacements will be taken into account. We may then reduce the expression for the aerodynamic load such as

$$\int_{x_{\text{sep}}^o}^{x_{\text{sep}}} \mathbf{f}_a \, \mathrm{d}s = \mathbf{n}(p_{\text{atm}} - p_{\text{sep}})(x_{\text{sep}} - x_{\text{sep}}^o) \tag{5}$$

where x_{sep}^o corresponds to the initial shock position and $\mathbf{n}$ the time dependent normal vector external to the wall. Written in a finite element context, we obtain

$$\langle \delta W \rangle \{F\} = \int_{x_{\text{sep}}^o}^{x_{\text{sep}}} \delta \mathbf{w}.\mathbf{n}(p_{\text{atm}} - p_{\text{sep}}) \, \mathrm{d}S = \langle \delta W \rangle [K_{\text{aero}}] \{W\} \tag{6}$$

with $\langle \delta W \rangle$ the global nodal value of test-function.

Damping effects due to material or to external devices have been neglected. Recalling Equation (2), it consists in choosing

$$[C_{\text{aero}}] = [0] \quad \text{and} \quad [K_{\text{aero}}]\{W\} = \frac{\mathfrak{B}}{-(\mathrm{d}p_\infty/\mathrm{d}x)_J} \begin{Bmatrix} n_x \\ n_y \\ 0 \end{Bmatrix}_J \left. \frac{\partial w_n}{\partial s} \right|_J \tag{7}$$

where J is the index of the node located at x_{sep}^o, n_x and n_y the normal vector components (see Figure 4). $\mathfrak{B}$ defines the shifting coefficient [9] for the pressure, given by

$$\mathfrak{B} = \frac{p(x,\mathbf{w}) - p_\infty^o(x)}{P_{\text{c}}(\partial w_n/\partial s)} \tag{8}$$

where P_{c} is the chamber pressure.

Equation (3) may be transformed in a classical eigenvalue problem by using the following decomposition form:

$$\{W(t)\} = \{\bar{W}_j\} \mathrm{e}^{\mathrm{i}\Omega_j t}$$

where Ω_j is the jth aeroelastic frequency associated to the eigenvector $\{\bar{W}_j\}$. It leads to the following free vibration model:

$$(([K] - [K_{\text{aero}}]) - \Omega_j^2 [M])\{\bar{W}_j\} = \{0\} \tag{9}$$

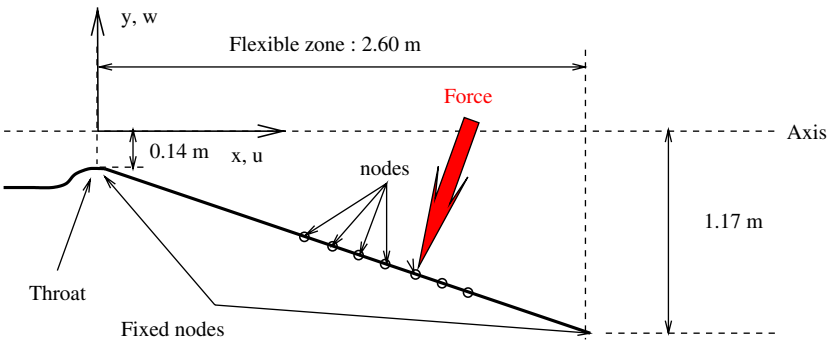

Figure 4. Model for flexible nozzle.

The evolution of the aeroelastic frequency profiles, $\Omega_j(x_J)$, of the structure is then obtained in conducting a classical calculation of the eigenmodes for each position of the shock (according to x_J with nodal index J) along the flexible part of the rocket engine. Projecting Equation (9) on the M-orthonormal eigenvectors $\{\bar{W}_j\}$, it leads to

$$\Omega_j^2 = \langle \bar{W}_j \rangle [K - K_{\text{aero}}] \{\bar{W}_j\} \tag{10}$$

We will call $[X]$ the global set of eigenvectors of the structure

$$[X] = [\{\bar{W}_1\} \ldots \{\bar{W}_j\} \ldots] \tag{11}$$

2.2. *Extension of the model to dynamic instabilities*

Pekkari's model considers that the eigenvectors $\{\bar{W}_j\}$ remain unchanged with regards to the shock position, only the eigenvalues $\Omega_j(x_J)$ being changed. However, the updating of the eigenvectors for each new shock position permits to observe coalescing frequencies phenomena analogous to those encountered in a flutter behaviour. This constitutes what we call the extended model that has been part of previous works [20]. The main drawback is the necessity to reconduct the eigenvectors calculation for each shock position (Equation (9)). However, it is possible in such a way similar to modal decomposition, to only consider the first eigenvectors in order to reduce calculation cost.

The global process used to obtain aeroelastic frequencies function of initial shock position may be decomposed as follows:

Parameters initialization and global data calculations:

- Calculation of pressure separation: $p_{\text{sep}} = \eta \times p_{\text{atm}}$.
- Assembling of $[K]$ and $[M]$.
- Pekkari's model: Computing of $[X]$.

Eigenvalues calculation:
J-loop on nodes located on $x_{\text{sep}} = x_J$

1. Extraction of shock position x_J.
2. Calculation of corresponding chamber pressure such as $p(x_J) = p_{\text{sep}}$.

Table I. Material properties.

Young modulus	Thickness	Poisson coefficient	Mass density
2.2×10^{11} N/m^2	1×10^{-2} m	0.0	2000 kg/m^3

Table II. Fluid properties.

Range for P_c (Pa)	T_c (K)	Range for shock position (m)	$\eta = p_{atm}/p_{sep}$	p_a (Pa)
$[0.5–6.5] \times 10^5$	2400	[0.1–2.55]	15.5	10^5

3. Calculation of $\mathfrak{B}$ (Equation (8)).
4. Assembling of $[K_{aero}]$ (Equation (7)).
5. Case of:
   - Pekkari's model: computing of $\Omega_j(x_J)$ for $j = 1, \ldots, N$ (Equation (10)).
   - Extended model: computing of $\Omega_j(x_J)$ and $\{\bar{W}_j\}$ for $j = 1, \ldots, N$ (Equation (9)).

End of J-loop

2.3. *'Analytical' validation of the extended stability model*

Both models can be tested by directly introducing the forcing term given by Equation (6) in a structural analysis code. The objective is to verify the instabilities predicted by each model for given material properties.

The structure code is based on the finite element method and will be described in a next subsection. It solves the system (Equation (1)) by using a Newmark scheme for the time discretization. The only modification consists in directly applying the solicitation (Equation (6)) after extracting the nodal displacements of the previous time step.

The domain of calculation is illustrated in Figure 4. It consists on a two-dimensional geometry with dimensions of a Vulcain class engine. However, in order to reduce two-dimensional effects, the profile of the nozzle has been chosen straight instead of parabolic. Only the divergent part is supposed flexible and is meshed using two-node beam elements. The mesh is made of 40 uniformly distributed nodes.

The material and fluid properties are respectively given in Tables I and II. The value given to the separation criterion (p_{atm}/p_{sep}) has been obtained from previous two-dimensional fluid calculations on the same domain. One may also show that stability results are very little dependent on the value given to this separation criterion.

The results obtained from the Pekari's model (Equation (10)) for each nodes corresponding to an initial shock position, are presented in dashed lines in Figure 5. The results obtained from the extended version (Equation (9)) are presented in Figure 5 in continuous lines.

We can make the following observations:

- For an initial position surrounding $x_{sep} \approx 0.8$ the first natural mode collapses with the zero-axis expressing a buckling effect. This behaviour is also reported in using the Pekkari's model;

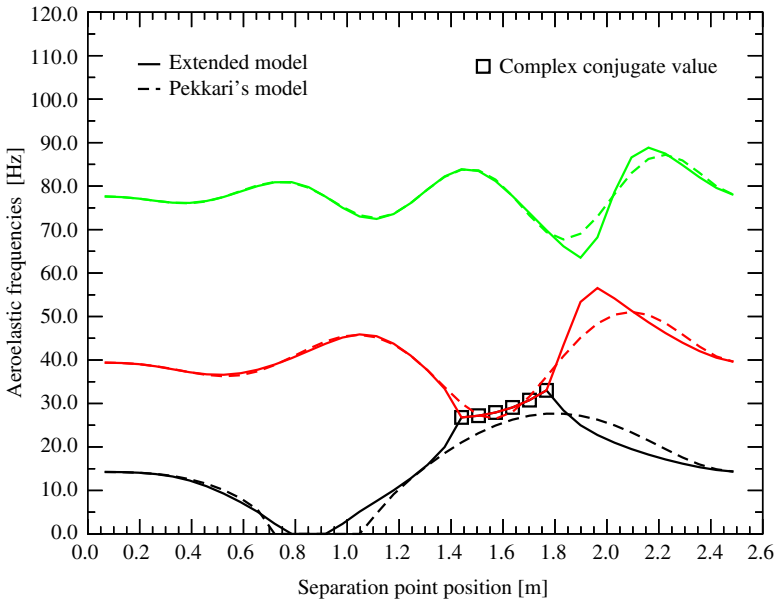

Figure 5. Analytical profiles for the first three modes.

- For x_{sep} belonging to the range [1.4–1.8], the first two natural modes collapse to complex conjugate eigenfrequencies. This expresses a dynamical instability similar to *flutter*. This case is not observed with Pekkari's model for which all frequencies remain real. It is due to the fact that for this model, eigenvectors used for modal projection are supposed unchanged and prevent this instability to appear. However, both models remain close of the global trend.

Remark
For a smaller Young modulus (results not shown here) that strengthens the collapsing modes effect, we observe for the Pekkari's model that the first two natural modes pass each other with no mutual interaction as swapping-modes.

The third calculation corresponds to an analytical validation of these previous results in introducing the forcing form (Equation (6)) into a structure code dedicated to dynamic simulation. The calculation has been conducted in applying the solicitation on several nodes to obtain the results presented in Figures 6–8.

For each case, we represent on the upper graph the temporal evolution of the radial displacement taken at the considered point. The time step has been taken equal to $\Delta t_s = 1.10^{-4}$ s and 2000 steps have been conducted. The lower graph is the spectrum obtained from a 'Fast Fourier Transform' (using the Matlab function): it is applied to the temporal signal of the radial displacement.

These results show the frequencies deviation forecasted by the stability model and confirm the coalescing effect between the first two modes and its exponential growth typical of the

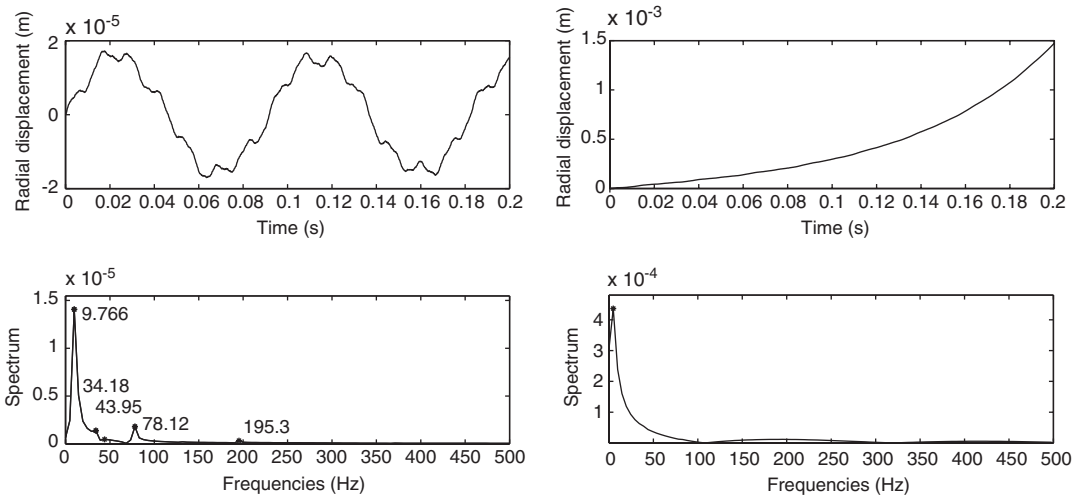

Figure 6. Results for $x_{sep} = 0.45$ and 0.85 m.

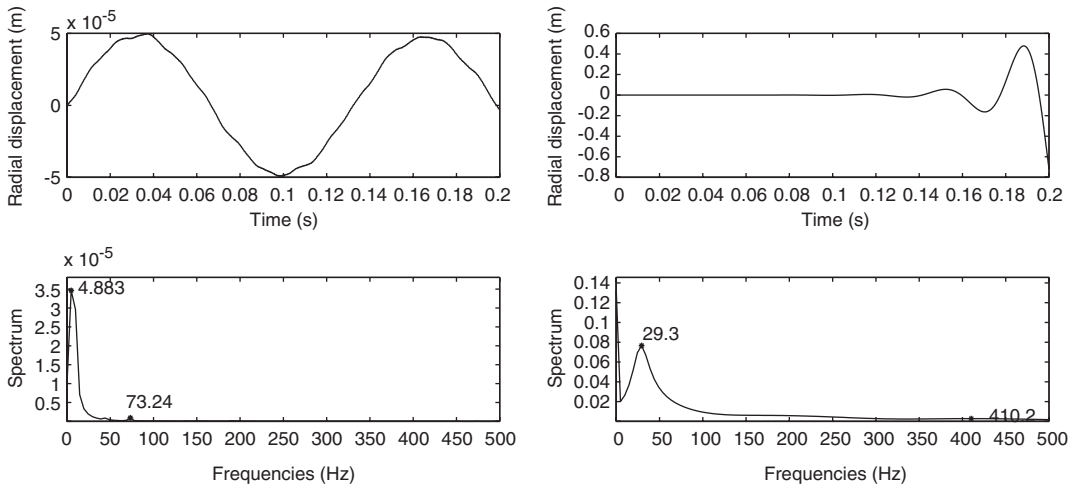

Figure 7. Results for $x_{sep} = 1.10$ and 1.54 m.

dynamical instabilities for the case $x_{sep} = 1.54$ m. This clearly concludes the necessity to use the extended model to determine aeroelastic frequencies. Tendencies predicted by both models being similar, it may be suggested to first conduct Pekkari's model and then, to conduct extended model for nodes where several frequencies show tendency to collapse.

However, these results do not constitute a complete validation because of the introduction of the particular form of the solicitation. In the following sections we will attach ourselves to validate the stability model in a more objective way in taking two different codes, respectively, dedicated for fluid and structure calculations and letting them proceed to their own coupling.

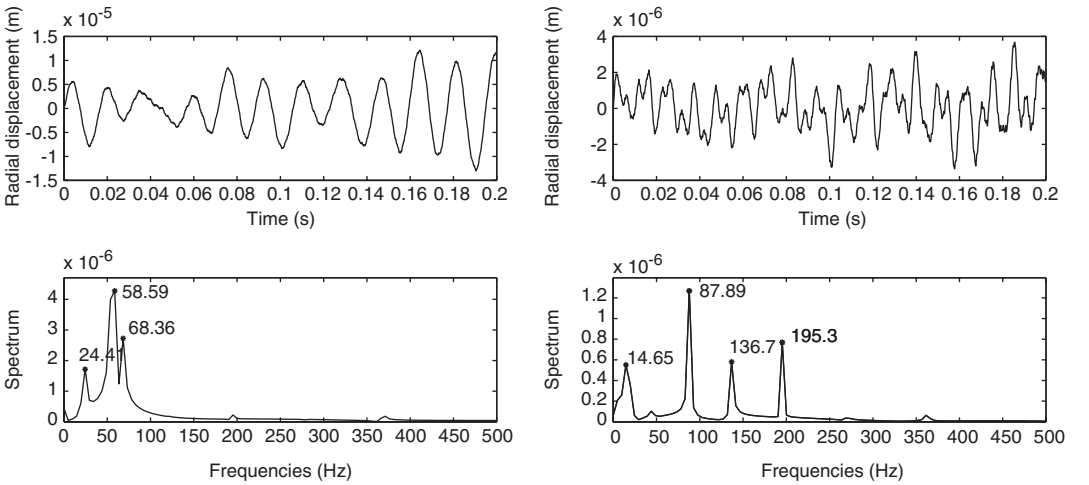

Figure 8. Results for $x_{\text{sep}} = 1.94$ and 2.20 m.

3. NUMERICAL MODEL FOR FLUID–STRUCTURE INTERACTION

The principle of the coupling is that developed primarily during work referred in Reference [20]. It consists of two codes dedicated to compute the structure deformation and the fluid flow, respectively.

3.1. Structure calculation

A finite element technique is used for space discretization of the flexible structure. For general cases including geometric non-linearities, it leads to the non-linear system

$$[M]\left\{\frac{\partial^2 u}{\partial t^2}\right\} + \{f_{\text{int}}(u,t)\} - \{f_{\text{ext}}\} = 0 \tag{12}$$

where $[M]$ is the global mass matrix, $\{u\}$ the nodal displacements vector, $\{f_{\text{int}}(u,t)\}$ the non-linear internal efforts, and $\{f_{\text{ext}}\}$ the external forces resulting from aerodynamical coupling.

Main characteristics of the solver are:

- A *Total Lagrangian Formulation* is employed to calculate the deformations of a flexible structure under large displacements hypothesis [25];
- The resolution of the resulting non-linear system is obtained using a Newton–Raphson iterative method [26, 27];
- Two finite elements are proposed in geometrical non-linearities assumptions, a two-dimensional two-nodes beam element and an axisymmetric shell element [11, 28, 29];
- An implicit Newmark scheme is used for temporal resolution of dynamical terms.

3.2. *Fluid flow calculation*

The global set of equation governing inviscid and compressible fluid flow on a two-dimensional moving domain are given by

$$\frac{\partial}{\partial t}\{JU\} + J\left(\frac{\partial\{F_x\}}{\partial x} + \frac{\partial\{F_y\}}{\partial y}\right) = 0 \tag{13}$$

where $\{U\}$ are the conservative variables, $\{F_x\} = \{F_{cx}\} - w_x\{U\}$ the convective flux along x-direction, and $\{F_y\} = \{F_{cy}\} - w_y\{U\}$ the convective flux along y-direction
with:

$$\{U\} = \begin{pmatrix} \rho \\ \rho u \\ \rho v \\ \rho e \end{pmatrix}, \quad \{F_{cx}\} = \begin{pmatrix} \rho u \\ \rho u^2 + p \\ \rho uv \\ (\rho e + p)u \end{pmatrix}, \quad \{F_{cy}\} = \begin{pmatrix} \rho v \\ \rho uv \\ \rho v^2 + p \\ (\rho e + p)v \end{pmatrix} \tag{14}$$

with ρ the mass density, u and v, respectively, the components of fluid velocity in (x, y) system, e the total energy per unit of mass and p the local pressure given by the law of perfect gas

$$p = \rho rT = (\gamma - 1)(\rho e - 1/2\rho(u^2 + v^2))$$

with the temperature T, $\gamma = 1.4$ and $r = 287u.SI$. The variables (w_x, w_y) represent the local velocity components of the domain. The variable J defines the local Jacobian that corresponds to the determinant of Jacobian matrix. This one expresses the transformation relations between a fixed and a moving space coordinates system.

Main characteristics of the solver are:

- A triangular finite element is used for the spatial discretization. A linear approximation is considered for all variables;
- An explicit Lax–Wendroff scheme is used for temporal discretization [30] with a shock capturing technique called *Flux Corrected Transport* [31] in zones where positivity is not ensured (presence of shocks for example);
- In order to ensure geometrical compatibility between both fluid and structure meshes, and to avoid excessive mesh distortion, a dynamic mesh technique is used to adapt fluid mesh to wall deformation. A discrete geometric conservation law is applied to ensure the same precision order and stability property of the solver obtained in the case of a rigid mesh [32]. From a practical point of view, it consists on integrating fluid flow equations on a mesh generated at mid-step between two successive time step t^n and t^{n+1} [28];
- A decomposition domain technique is used to parallelize the flow solver in order to significantly reduce CPU cost. The partitioning tool CHACO [33] is used to decompose the initial mesh on 'N' sub-meshes. Nodes are duplicated on boundaries between each subdomain in order to compute fluxes the same way than in the single mesh case (see Figure 9). Due to the iterative process for solving nonlinear fluid flow, common data are exchanged between sub-domains before each flux calculation.
- Stability is ensured using a CFL criterion [34].

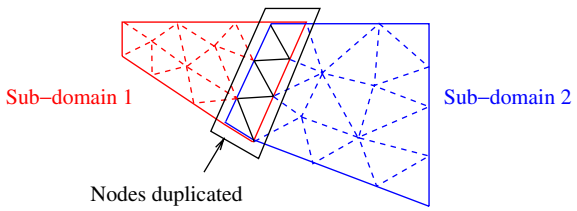

Figure 9. Domain decomposition with duplication of nodes between neighbouring sub-domains.

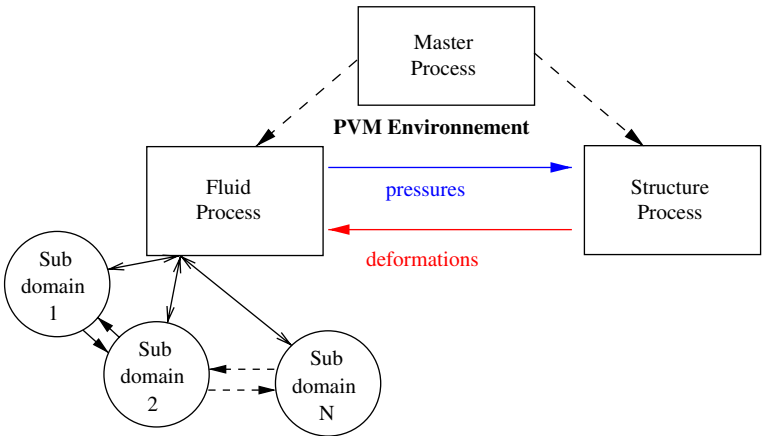

Figure 10. Message passing between fluid and structure codes.

3.3. *Coupling*

Fluid structure calculations are obtained in coupling both codes such as:

- In order to preserve modularity aspects of each code taken separately, the coupling is done in establishing a 'message-passing' between solvers by using parallel tools offered by Parallel Virtual Machine (PVM) routines [35, 36] (see Figure 10);
- The exchanged data during calculations consist of the wall pressure distribution and time step from the fluid code to the structure one, and the update of the flexible boundaries common to both codes from the structure to the fluid;
- The characteristic times being different by several orders of magnitude between both codes (implicit structure code and explicit fluid code), the updating of wall conditions is made using a sub-cycling coupling scheme and thus carried out every $N_{\mathrm{f/s}}$ fluid steps;
- Several sub-cycling schemes may be employed depending on the required accuracy (with CPU considerations) and the type of common wall boundary at the interface. Usually, kinematic compatibility and energy conservation are not both ensured simultaneously. The data exchange is here based on a discontinuous coupling scheme (see Figure 11), which although does not preserve the kinematic compatibility between the meshes of the fluid and the structure, makes possible to better ensure the transfer of energy and momentum between the two physics [18].

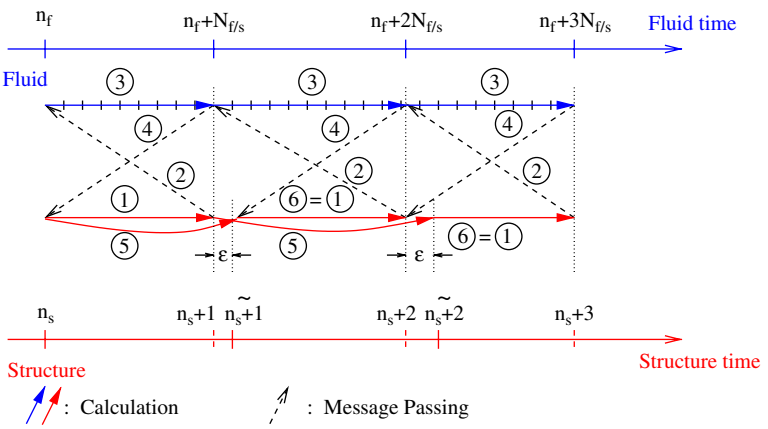

Figure 11. Discontinuous fluid–structure coupling scheme.

The exchange process illustrated Figure 11 must be read as follows:

1. From time station n_s, we conduct a single time step for structure solver to update displacements, velocities, strains, etc. New position corresponds now to time station $n_s + 1$.
2. Transfer to the fluid code of the informations based on the new structure state.
3. From time station n_f, we conduct $N_{f/s}$ consecutive fluid time steps to update all fluid data on the mesh and reach time station $n_f + N_{f/s} = n_s + 1$. The fluid mesh is progressively deformed in order to match both fluid boundary and new structure deformation.
4. Transfer to the structure code of the new parietal pressure profile.
5. Structure deformation is then updated in accordance to these new fluid data in conducting a new calculation from previous time station n_s.
6. A new cycle begins.

4. COMPARATIVE STUDY OF BOTH MODELS

The objective here is to compare results obtained from full fluid–structure calculations with results predicted by the extended stability model (given in Figure 15).

We show in Figure 12, the calculation domain with the corresponding boundary conditions. Material properties remain unchanged and given in Table I. The fluid boundary conditions are based on the characteristics theory for both the entrance and exit of the domain. A slip condition is applied to the flexible wall and a symmetry condition for the X-axis. Concerning the flexible structure, both ends of the wall are supposed fixed.

During the mesh adaptation process, mesh velocities are obtained using linear interpolation in both direction as shown in Figure 13:

- For each interior moving node, locate its radial projection on flexible boundary and search the two neighbouring nodes whose velocities are known, $\mathbf{w}^{up}$ and $\mathbf{w}^{down}$;
- Calculate $\mathbf{w}^{project}$ of projected point by using linear interpolation between $\mathbf{w}^{up}$ and $\mathbf{w}^{down}$;

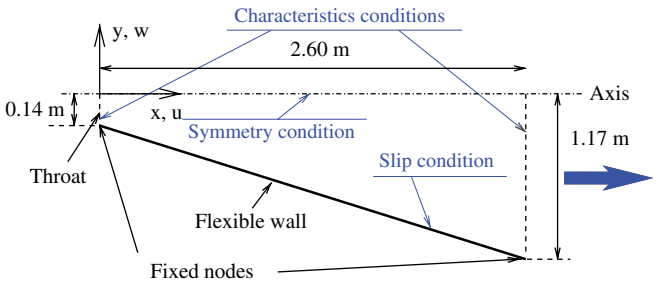

Figure 12. Calculation domain.

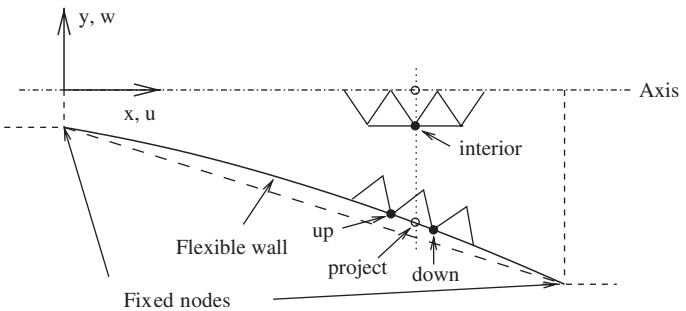

Figure 13. Mesh adaptation.

- Obtain interior node velocity by linear interpolation between $\mathbf{w}^{\text{project}}$ and zero-velocity on symmetrical axis.

A calculation series was carried out for three different mesh sizes:

- 5000 nodes and 10^4 triangular elements of size equal to $\Delta x = 2$ cm,
- 20 000 nodes and 39×10^3 triangular elements of size equal to $\Delta x = 1$ cm,
- 80 000 nodes and 150×10^3 triangular elements of size equal to $\Delta x = 0.5$ cm.

The frequency differences between calculations conducted on the different meshes ranging from 1 to 3 Hz, it has been decided to only consider the second mesh described above for all future calculations.

A chamber pressure ranging from 1.5 to 6 bar permits to adjust the shock position along the divergent, making thus possible the study of the aeroelastic response for different initial positions.

Each coupling calculation is conducted as follows (see Figure 14):

1. Choice of a pressure chamber P_c to control the separation shock position.
2. The fluid calculation is conducted until convergence is reached (generally in 20 000 steps). For this step, the structure is supposed rigid.

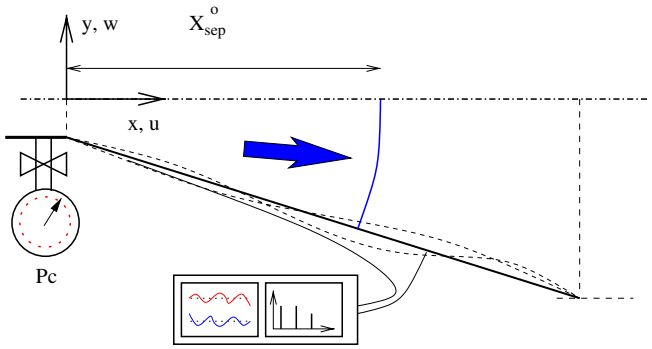

Figure 14. Calculation of aeroelastic frequencies vs shock position.

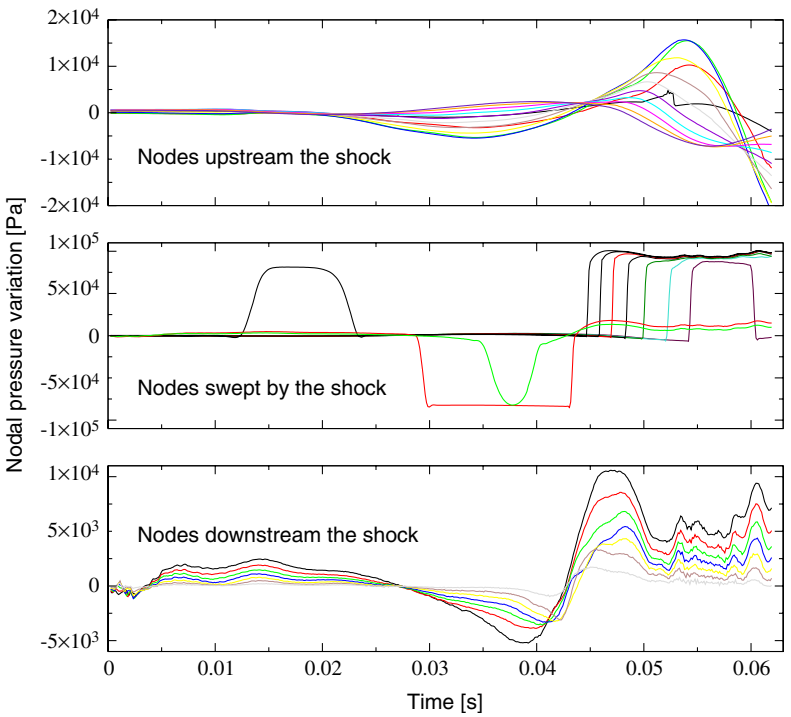

Figure 15. History of pressure variations for different locations of nodes: case $x^{o}_{sep} = 1.70\,\mathrm{m}$.

3. The parietal pressure profile is then stored ($P(x,0)$), and flexibility is given back to the structure.
4. Coupling calculation is conducted. We extract $P(x,0)$ from the instantaneous parietal pressure profile before sending to the structure code to update the parietal deformation (stability assumption). Nodal pressure and structural displacement are stored for different stations during the coupling process (see Figure 15). Each curve corresponds to a different node.

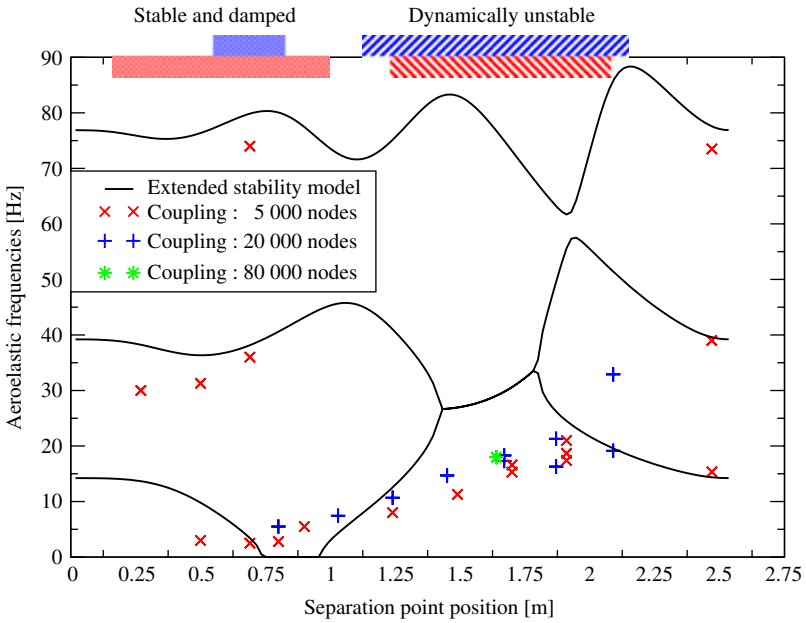

Figure 16. Comparative between analytical and numerical solutions.

5. A Fast Fourier Transform is then applied to the stored pressure and displacement signals to extract response frequencies (see Figure 16).

In Figure 16 we display results obtained on the one hand from the extended stability model (full line) and on the other hand, the results obtained by the fluid–structure calculation (symbols '$\times\times$' and '$+\!+$'). We give in X-coordinate, the position of the shock in the rocket engine and in Y-coordinate the evolution of the first three frequencies of the structure. Several remarks:

- The stability model predicts a first zone of static instability ($0.75\ \text{m} < x_{\text{sep}} < 0.90\ \text{m}$) corresponding to the cancellation of the first frequency with a negative imaginary part (buckling effect). There follows a second zone of dynamic instability ($1.40\ \text{m} < x_{\text{sep}} < 1.80\ \text{m}$) with coalescing between the two first frequencies that become complex and conjugate (similar to flutter effect).
- Coupling calculation never detects any buckling effect. However, it detects a first frequency fall to 3 Hz with a high damped response of the structure.
- The second unstable zone is perfectly detected. This zone proves to be wider but for a coalescing frequency equal to 60% the predicted one!
- The variations in results obtained with different sizes of mesh prove to be weak.
- In order to test the limits of the fluid code in terms of spatial precision (2nd order in space and time), fluid calculations with a higher order scheme (WENO 5th order) [23] have been conducted and show similar results.
- For extreme position of the shock (near the throat or the exit) one finds a good agreement between the values of the first three natural frequencies.

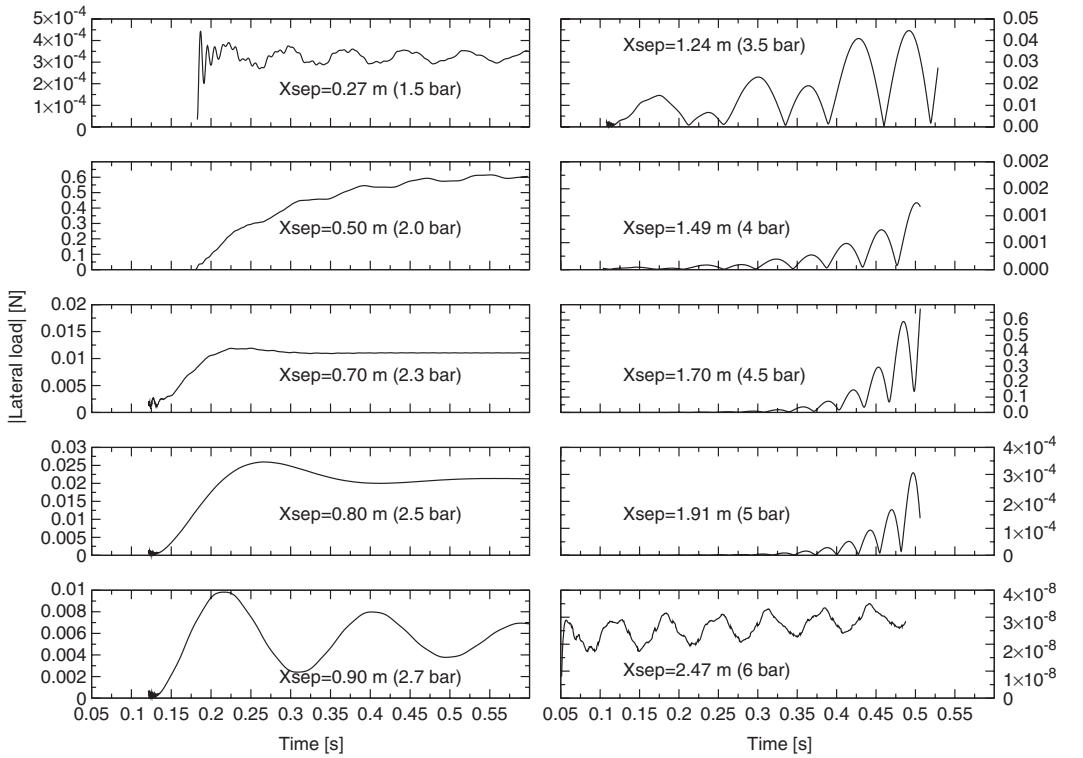

Figure 17. Normalized magnitude of side loads.

In first conclusion, the two models prove to be similar from a qualitative point of view (presences of zones of instabilities) but present differences in frequency values.

We also show in Figure 17 the absolute value of the side load function of the time. This latter is obtained from pressure integration along the flexible wall. Each graph corresponds to a different initial shock position along the divergent zone. For a position ranging from 0.27 to 0.90 m, the structure has a stable response with a highly damped effects for $X_{\text{sep}} = 0.50$ m.

For a shock position ranging from 1.24 to 1.91 m, the structure undergoes a dynamic instability such as flutter phenomena, the only frequency being able to be interpreted like the coalescing of the two first frequencies. We illustrate in Figure 18 the pressure contours at the beginning and at the end of the coupling process for the case $x^{o}_{\text{sep}} = 1.70$ m. Both figures clearly show the shock displacement in agreement with the wall deformation.

The last calculation corresponding to a shock position such as $X_{\text{sep}} = 2.47$ m shows a return to a stable behaviour that is developed on the first natural frequencies.

The coupled calculations on various sizes of mesh showing weak differences, it tends to call into question the model of stability and its tendency to over-estimate the frequency shift. A finer study of the $\mathfrak{B}$ term (controlling the shifting) present in Equation (7), makes it possible to bring brief replies. Recent work [10] completed by the original team of the Pekkari's model tends to confirm this observation.

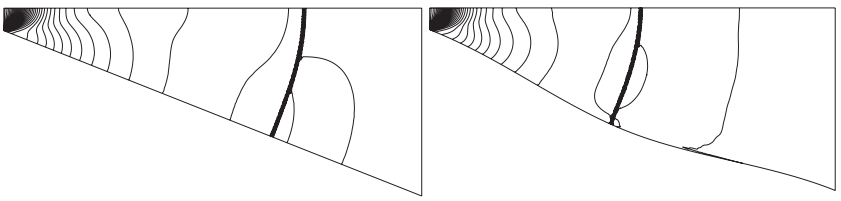

Figure 18. Pressure contours resp. at the beginning and at the end of the coupling process : case $x^o_{sep} = 1.70$ m.

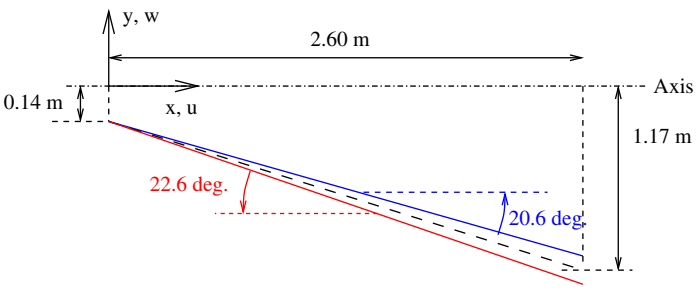

Figure 19. Modified configurations.

In order to validate this fact, two different ways of investigation have been studied:

- A coupling calculation with a Young modulus reduced by 30% (that gives an increased theoretical buckling zone ranging between 0.5 and 1 m) finally made possible to detect a buckling effect, which confirms the model's tendency to over-estimate the spectral shift.
- Two fluid calculations have been carried out on geometrical configurations similar to the original one (Figure 19) and presenting each one an opening modified respectively by $\pm 1°$.

After extraction of the pressure profile resulting from one of these modified configurations, $p(x, \mathbf{w})$, and from the initial one, $p^o_\infty(x)$, the coefficient $\mathfrak{B}$ has been calculated using Equation (8) recalled below

$$\mathfrak{B} = \frac{p(x, \mathbf{w}) - p^o_\infty(x)}{P_c(\partial w_n/\partial s)} \quad \text{with} \quad \frac{\partial w_n}{\partial s} = \tan(\pm 1°) \text{ and } P_c = 8 \text{ bar}$$

and compared with the one obtained from the stability model (Figure 20). The tendency of the stability model to over-estimate the shift in comparison with results extracted from 2D calculations clearly appears. The coefficient $\mathfrak{B}$ may thus be a way of investigation to improve the predictive qualities of the stability model. A proposal is to conduct 2D calculations, to calculate its profile from Equation (8) and put it into the stability model.

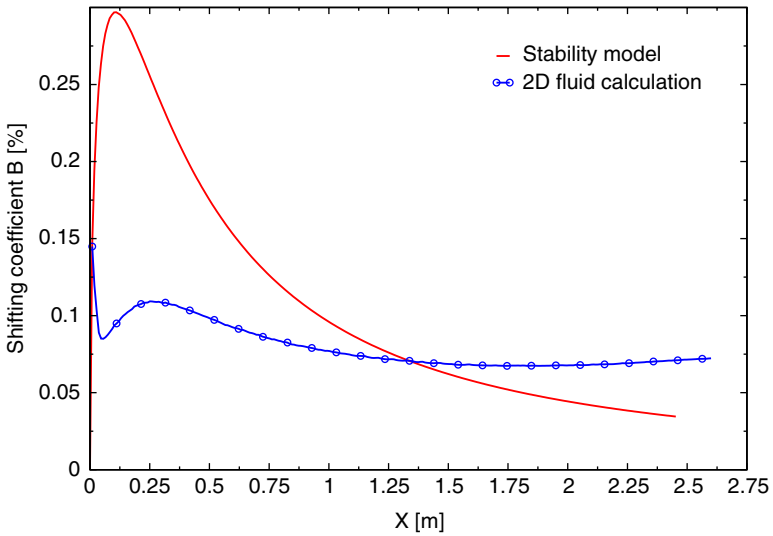

Figure 20. Shifting aeroelastic coefficient.

5. CONCLUSION AND PERSPECTIVES

A comparative study has been conducted along this work to show the current limits of a model dedicated to the stability analysis of an over-expanded rocket engine. Numerical tools for fluid–structure calculations have been briefly described in order to test the limits of the stability model. Its tendency to over-predict the frequency shift but also its capacity to detect static and dynamic instabilities depending on the initial separation shock position in the divergent zone has been clearly observed. However, once the instability has been reached, it will be necessary to conduct structure calculations including large displacement effects in order to verify if the instability tends to a limit cycle oscillation or still growths.

In conclusion, to allow an accurate understanding and prediction of the aeroelastic effects, the extended stability model to dynamical instabilities requires a correction. For the buckling case, this one can be estimated in correcting coefficient $\mathfrak{B}$ from 2D fluid calculations carried on openings modified geometries. This procedure may be improved from a local point of view (deformation $\partial W_n/\partial s$) to eliminate the cumulated effects generated upstream the current shock position. But this approach seems to be badly adapted to readjust a frequency coalescing effect.

Current works are consisting in extending fluid–structure calculation to a complete divergent nozzle with two distinct deformable walls in order to induce a possible dissimetry of the flow and side-load effects.

ACKNOWLEDGEMENTS

These works have been partly realized with the support of computer resources (PILCAD — Plateforme Inter-Laboratoires de CAlcul Distribués) financed as part of an ANVAR support and Heudyasic and Roberval laboratories (University of Technology of Compiègne — France). They also currently con-

cern research activities in collaboration with researchers of the LMFN (Laboratory of Numerical Fluid Mechanics) in Rouen (France).

REFERENCES

1. Mouronval AS, Hadjadj A. Numerical study of the starting process in a supersonic nozzle. *CIMNE*, *West East High Speed Flow Fields*, Barcelona 11–15, 2002.
2. Summerfield M, Foster C, Swan W. Flow separation in overexpanded supersonic exhaust nozzles. *Jet Propulsion* 1954; **24**(9):319–320.
3. Schmucker RH. Flow processes in overexpanded chemical rocket nozzles—Part I. *NASA Report-77396*, 1984.
4. Reed D, Hidalgo J. Fluctuating pressure analysis of a 2-D SSME nozzle air flow test. *Workshop for Computational Fluid Dynamic Applications in Rocket Propulsion and Launch Vehicle Technology*, Huntsville, Alabama, 26 April, 1995.
5. *European Seminar on Rocket Nozzle Flows*, 1998.
6. Etude du Comportement Dynamique du Divergent du Moteur VULCAIN. *Laboratoire de Mécanique des Structures secteur ENSAM*, *Université Paris VI - Dossier 60737*, 1996.
7. Hadjadj H. Analyse physique et simulation numérique des ecoulements compressibles; application aux tuyères de propulseurs. *Thesis*, LMFN-CORIA, Université Rouen - France, 1997.
8. Frey M, Hagemann G. Flow separation and side-loads in rocket nozzles. *AIAA 99-2815*.
9. Östlung J. Flow processes in rocket engine nozzles with focus on flow separation and side-loads. *Royal Institute of Technology*, *Department of Technology*, S 100–44, Stockholm, Sweden, 2002.
10. Östlung J, Damgaard T, Frey M. Side-load phenomena in highly overexpanded rocket nozzles. *37th AIAA/ASME/SAE/ASEE*, *Joint Propulsion Conference and Exhibit*, Salt Lake City, 8–11 July, 2001.
11. Lefrançois E, Dhatt G, Vandromme D. Fluid–structural interactions with applications to rocket engines. *International Journal for Numerical Methods in Fluids* 1999; **9**(30):865–895.
12. Pekkari LO. Aeroelastic stability of supersonic nozzles with separated flow. *AIAA*, *29th Joint Propulsion Conference and Exhibit*, Monterey, CA, 28–30 June, 1993.
13. Dowell EH. *Aeroelasticity of Plates and Shells*. Noordhoff International Publishing: Leiden, 1975.
14. Fung YC. *An Introduction to the Theory of Aeroelasticity*. Wiley: New York, 1958.
15. Bisplinghoff RL, Ashley H. *Principles of Aeroelasticity*. Wiley: New York, 1975.
16. Kondo N, Tosaka N *et al*. Numerical simulation for coupled system of viscous flow and elastic shell. *Numerical Methods in Laminar and Turbulent Flow*, vol. 4 (Part 2), 1987; 1798.
17. Le Tallec P, Mouro J. Structures en grands déplacements couplées à des fluides en mouvement. *INRIA — No 2961*, 1996.
18. Piperno S, Farhat C, Larrouturou B. Partitioned procedures for the transient solution of coupled aeroelastic problems. Part I: model problem, theory and two-dimensional application. *Computer Methods in Applied Mechanics and Engineering* 1995; **9**(124):79–112.
19. Tuovila WJ, Land NS. Experimental study of aeroelastic instability of overexpanded rocket nozzle extensions. *NASA TN D-4471*, 1968.
20. Lefrançois E, Dhatt G, Vandromme D. Numerical study of the aeroelastic stability of an overexpanded rocket nozzle. *Revue européenne des éléments finis* 2000; **9**(6):727–762.
21. Shall E, Lardat R, Dervieux A, Koobus B, Farhat C. Aeroelastic coupling between a thin divergent and high pressure jets. *Revue européenne des éléments finis* 2000; **9**(6):835–851.
22. Naudin P. Etude de Faisabilité d'une Tuyère Souple à Echelle Réduite. *ONERA*, *Doc. RTS 2/2336 DDSS/Y*, 1998.
23. Mouronval AS. Etude numérique des phénomènes aéroélastiques en aérodynamique supersonique. Application aux tuyéres propulsives. *Thesis*, LMFN-CORIA, Université Rouen — France, 2004.
24. Ashley H, Zartarian G. Piston theory—a new aerodynamic tool for the aeroelastician. *Journal of the Aeronautical Sciences* 1956; **23**(12):1109–1118.
25. Dhatt G, Fafard M. Mécanique non linéaire. *Institut Pour la Promotion des Sciences de l'Ingénieur — Paris*, 1995.
26. Dhatt G, Fafard M. Résolution de problèmes non linéaires. *Institut Pour la Promotion des Sciences de l'Ingénieur - Paris*, 1995.
27. Ammar S. Résolution des problèmes non linéaires. *Thesis*, Département Génie Mécanique, Université Laval, Québec, 1996.
28. Lefrançois E, Dhatt G, Vandromme D. Modèle numérique de couplage fluide–structure avec applications aux moteurs fusée. *Revue européenne des éléments finis* 2000; **9**(8):159–199.
29. Dhatt G, Fafard M. Modélisation des coques en grandes rotations. *Institut Pour la Promotion des Sciences de l'Ingénieur, Paris*, 1995.

30. Lax PD, Wendroff B. Systems of conservation laws. *Communications on Pure and Applied Mathematics* 1960; **9**(13):217–237.
31. Boris JP, Book DL. Flux-corrected transport, I. SHASTA, a fluid transport algorithm that works. *Journal of Computational Physics* 1973; **9**(135):172–186.
32. Guillard H, Farhat C. On the significance of the geometric conservation law for flow computations on moving meshes. *Computer Methods in Applied Mechanics and Engineering* 2000; **190**:1467–1482.
33. Hendrickson B, Leland R. *The CHACO User's Guide*, *version 2.0*. Sandia National Laboratories: Albuquerque, NM, 1995.
34. Mac Cormack RW. *Numerical Computation of Compressible Viscous Flow*. Stanford University Course, 1992.
35. Geist A, Beguelin A *et al. PVM 3 User's Guide and Reference Manual*. Oak Ridge National Laboratory, 1994.
36. Kessy E. Décomposition de domaine et calcul parallèle distribué: application à la mécanique des fluides. *Thesis*, LMFN-CORIA, Université Rouen, France, 1997.

